PHYSICS

Electron confinement–induced plasmonic breakdown in metals

Prasanna Das[1], Sourav Rudra[1], Dheemahi Rao[1], Souvik Banerjee[1], Ashalatha Indiradevi Kamalasanan Pillai[2], Magnus Garbrecht[2], Alexandra Boltasseva[3], Igor V. Bondarev[4], Vladimir M. Shalaev[3], Bivas Saha[1,5]*

Plasmon resonance represents the collective oscillation of free electron gas density and enables enhanced light-matter interactions in nanoscale dimensions. Traditionally, the classical Drude model describes plasmonic excitation, wherein plasma frequency exhibits no spatial dispersion. Here, we show conclusive experimental evidence of the breakdown of plasmon resonance and a consequent metal-insulator transition in an ultrathin refractory plasmonic material, hafnium nitride (HfN). Epitaxial HfN thick films exhibit a low-loss and high-quality Drude-like plasmon resonance in the visible spectral range. However, as the film thickness is reduced to nanoscale dimensions, Coulomb interaction among electrons increases because of electron confinement, leading to the spatial dispersion of plasma frequency. With a further decrease in thickness, electrons lose their ability to shield the incident electric field, turning the medium into a dielectric. The observed metal-insulator transition might carry some signatures of Wigner crystallization and indicates that such transdimensional, between 2D and 3D, films can serve as a promising playground to study strongly correlated electron systems.

INTRODUCTION

Plasmons are quantized quasiparticles of collective free-electron oscillation in conductive medium, enabling light confinement at nanoscale dimensions (*1*–*4*). Plasmon resonance leads to intense optical absorptions and local field enhancement in nanostructures (*5*) and is used extensively for various applications such as photocatalysis (*6*), local heating (*7*), photovoltaics (*8*), sensing (*9*), microscopy (*10*), optical communications (*11*), and nonlinear optics (*12*). Traditionally, the classical Drude model is used to describe plasmon resonance, wherein the screened plasma frequency (ω_p) depends on the carrier concentration (n), effective mass (m^*), and the core dielectric constant (ε^{core}) of the medium. The Drude model has been used extensively to describe the plasmonic properties of metallic films and nanoparticles (*13*, *14*), doped semiconductors (*15*), layered materials such as graphene (*16*), and transition metal dichalcogenides in the visible-to-infrared (IR) spectral ranges (*17*). However, as ω_p does not exhibit any spatial dispersion (thickness dependence) according to the Drude model, the tunability of plasmon resonance can be achieved only with the changes in the doping concentration of semiconductors in the IR spectral ranges (*15*). For Drude metals exhibiting plasmon resonances in the visible spectral ranges, tuning the plasmon resonance is exceptionally challenging as the carrier concentrations cannot be varied readily.

However, a recent nonlocal Drude dielectric response theory based on the Keldysh-Rytova (KR) potential that incorporates electron confinement in a thin plasmonic medium predicts a spatial dispersion of the plasmon resonance and increased dissipative loss at the ω_p (Fig. 1, A and B) (*18*, *19*). The confinement theory further suggests that, in the limit where the dielectric constant (ε^{core}) of the medium is greater than the surroundings [substrate (ε_1^{core}) and superstrate (ε_2^{core})] and in ultrathin films (see the Supplementary Materials for details), the strong unscreened in-plane Coulomb potential confines carriers. Because of such electronic confinement, plasmonic metals lose their ability to respond to an incident electric field, turning effectively into a dielectric. Such breakdown of the plasmon oscillations in metals is analogous to the electric field–induced dielectric breakdown in insulators and could markedly alter plasmonic device performance (*20*). The momentum-averaged density of electronic states also qualitatively explains the plasmonic breakdown and the consequent electronic metal-insulator transition (MIT) (Fig. 1C). In the thick plasmonic films, the electron states are delocalized, and the Fermi energy (E_F) lies inside the conduction band, leading to their Drude-like metallic response. However, as the film thickness is reduced, the increased Coulomb interaction among charges localizes their states close to the E_F, leading first to transdimensional (TD) plasmonic medium (*21*) where the mobility edge (E_M; the energy that separates localized and nonlocalized states) is below the E_F and eventually to the plasmon resonance breakdown when more electron states are localized and the E_M shifts above the E_F. Because of the plasmonic breakdown, the material effectively becomes a dielectric, termed as KR insulator here. TD plasmonic materials and KR insulators are expected to unlock state-of-the-art applications that demand high transparency and dynamic tunability, as well as reveal unique phenomena related to unusual electromagnetic responses such as enhanced Purcell effect (*22*), resonant magneto-optical response (*23*), negative refraction (*24*), low-temperature ω_p drop-off (*25*), and altered near-field heat transfer (*26*).

The possibility of observing the electron confinement–induced plasmonic breakdown in metals is intriguing and could provide insights into the physical phenomena associated with strongly correlated systems in TD materials as well as means to control it. Thus far, experimental observation of the MIT in TD materials is challenging

[1]Chemistry and Physics of Materials Unit and International Centre for Materials Science, Jawaharlal Nehru Centre for Advanced Scientific Research, Bangalore 560064, India. [2]Sydney Microscopy and Microanalysis, The University of Sydney, Camperdown, NSW 2006, Australia. [3]Elmore Family School of Electrical and Computer Engineering, Purdue Quantum Science and Engineering Institute, and Birck Nanotechnology Center, Purdue University, West Lafayette, IN 47907, USA. [4]Department of Mathematics and Physics, North Carolina Central University, Durham, NC 27707, USA. [5]School of Advanced Materials and Sheikh Saqr Laboratory, Jawaharlal Nehru Centre for Advanced Scientific Research, Bangalore 560064, India.
*Corresponding author. Email: bsaha@jncasr.ac.in, bivas.mat@gmail.com

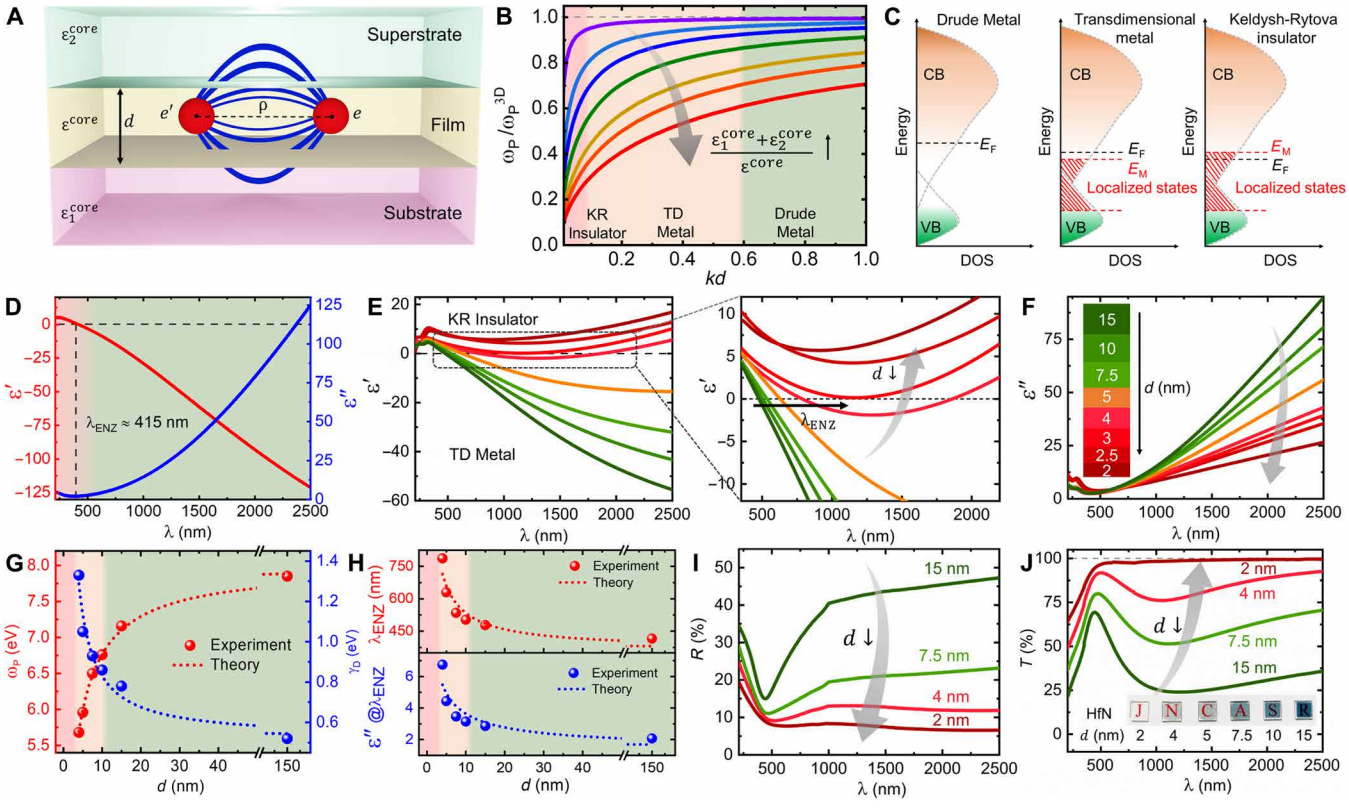

Fig. 1. Electron confinement–induced plasmonic breakdown in HfN. (**A**) Schematic of a plasmonic metal sandwiched between a substrate and a superstrate. As the film thickness (*d*) decreases, interaction potential among charges acquires an in-plane character and increases markedly, leading to electron confinement. (**B**) Because of the increased confinement, the plasma frequency (theoretically calculated) in transdimensional (TD) metals acquires a spatial dispersion and decreases with the reduced film thickness. The different colors represent the varying values of $\frac{\varepsilon_1^{core}+\varepsilon_2^{core}}{\varepsilon^{core}}$. As the value of $\frac{\varepsilon_1^{core}+\varepsilon_2^{core}}{\varepsilon^{core}}$ increases from 0.01 (violet) to 1 (red), the value of $\frac{\omega_p}{\omega_p^{3D}}$ decreases. (**C**) Schematic representing the localization of the electronic states due to electron confinement. CB, conduction band; VB, valence band; DOS, density of states. (**D**) The real (ε′) and imaginary (ε″) components of the dielectric permittivity of a thick HfN film. (**E**) The ε′ of HfN films as a function of thickness. The inset shows a clear redshift of the epsilon-near-zero (ENZ) wavelength (λ_{ENZ}) in the TD films. (**F**) The ε″ decreases with the decreasing film thickness at long wavelengths. (**G**) For the TD films, the plasma frequency (ω_p) and the Drude damping coefficient (γ_D) exhibit a spatial dispersion. (**H**) Variation of λ_{ENZ} and optical loss (ε″) at the ENZ wavelength (experimental and theoretical) with the film thickness. Thickness-dependent (**I**) reflection and (**J**) transmission spectra of HfN films. With increasing ε″ and γ_D, the reflection dip of the TD films spectrally broadens and shifts slightly due to the plasma frequency redshift. The transmission of films with thickness from 2 to 15 nm is represented with the "JNCASR" written below.

due to the materials' limitations. Traditionally, noble metals such as gold (Au) and silver (Au) are regarded as the best-known plasmonic materials for the visible spectral range. However, depositing ultrathin films of Au, Ag, or other noble metals is challenging as they exhibit island (Volmer-Weber) growths due to their large surface energies (1 to 2 J/m^2) (*27*). Moreover, noble metals are not structurally and morphologically stable at elevated temperatures (1000°C) and are incompatible with the complementary metal-oxide semiconductor process, limiting their practical applications (*28*). On the other hand, transition metal nitrides (TMNs) such as TiN and hafnium nitride (HfN) have emerged as an alternative plasmonic material to Au and Ag, respectively, and exhibit many interesting plasmonic properties (*28*, *29*). A spatial dependence of ω_p was recently demonstrated in TD epitaxial TiN films deposited on (001) MgO substrates (*30*). The studied TD TiN films retained their metallic characteristics even at a minimal thickness of 2 nm, without exhibiting plasmonic breakdown (*31*). However, unambiguous demonstration of the plasmonic breakdown and the MIT in epitaxial ultrathin metals could unlock unique electron confinement–related physical phenomena and pave the way for innovative optical and optoelectronic devices, especially in flat optics using metasurfaces. In this work, we present the conclusive experimental evidence of the electron confinement–induced plasmonic breakdown and a consequent MIT in an ultrathin refractory metal, namely, HfN.

HfN is an ambient-stable, corrosion-resistant TMN with a melting temperature of ~3600 K. HfN crystalizes in the rocksalt structure and exhibits a superconducting ground state with a transition temperature of ~5 to 10 K (*32*). HfN films exhibit a high electrical conductivity of ~3.7 ×10^4 Sm^{-1} and carrier concentration of ~6.6 × 10^{22} cm^{-3} (*33*). A long photoexcited carrier lifetime (*34*), large phononic bandgap (*35*), and high mechanical hardness have made HfN attractive for hot-carrier solar cell and tribology applications.

Thick HfN films representing the bulk limit and deposited on (001) MgO substrates exhibit high-quality and low-loss Drude-like plasmonic resonance in the 350- to 420-nm spectral range, which is comparable to the optical properties of noble metals. With an optimized deposition condition, recent research has also shown that thick HfN films exhibit a high solar reflectivity of 90% and IR

reflectivity of 95%, positioning them as an alternative plasmonic material to Ag for solar mirror and IR reflector applications (*33*, *36*). Notably, HfN exhibits a substantially higher Drude damping coefficient (γ_D) compared to TiN or Ag, attributed to stronger electron-phonon interactions, dislocations, grain boundaries, and defect scattering (see table S1 and sections II and V in the Supplementary Materials), making it a promising candidate for investigating confinement-related physical phenomena. In this study, we use the optimized deposition conditions (*33*) to deposit epitaxial, nominally single-crystalline, high-quality HfN films of varying thicknesses and explore electron confinement effects in the transdimensional regime.

RESULTS AND DISCUSSION

Epitaxial bulk (150 nm thick) and ultrathin (thickness from 2 to 15 nm) HfN films are deposited on (001) MgO substrates at 900°C substrate temperature using an ultrahigh vacuum magnetron sputtering (see the Supplementary Materials for details). The dielectric permittivity of the deposited films is measured with spectroscopic ellipsometry in the 210- to 2500-nm spectral range (see the Supplementary Materials for details). Results show that thick HfN film exhibits Drude-like plasmonic response with an epsilon-near-zero (ENZ) crossover wavelength [where the real part of the dielectric permittivity (ε') changes from positive to negative, thus crossing zero] at 415 nm (Fig. 1D). The ε' increases monotonically in negative direction and exhibits excellent metallic response, represented by high $|\varepsilon'|$ at long wavelengths. Similarly, the imaginary component of the dielectric permittivity (ε'') or material optical loss increases at long wavelengths due to free-electron Drude absorption. Low optical loss near the ENZ wavelength (λ_{ENZ}) leads to the high plasmonic figure of merit (*33*), long propagation length, and large decay length in HfN, as shown in section I of the Supplementary Materials.

However, as the thickness of the film is reduced, $|\varepsilon'|$ decreases progressively in the visible and near-IR spectral ranges (Fig. 1E), suggesting the reduced metallicity of the films. The ENZ wavelength exhibits a redshift from 478 nm in 15-nm-thick to 787 nm in 4-nm-thick films. Such spatial dispersion of the ENZ wavelength departs from the classical Drude metallic characteristics in HfN and arises because of electron confinement from enhanced interactions among charges in the TD films. When the thickness is reduced further (less than 4 nm), ε' becomes positive over the entire spectral range, thus exhibiting the breakdown of the plasmon resonance and the onset of the MIT. The crossover from the TD-plasmonic to KR-insulating regime can be obtained from the nonlocal Drude dielectric response theory that takes into account confinement effects in ultrathin films (see section II in the Supplementary Materials for details) (*18*, *19*, *23*), where ε' is expressed by the relation

$$\varepsilon^{core}\left[1-\frac{\left(\omega_p^{3D}\right)^2}{\left(\omega^2+{\gamma_D}^2\right)\left(1+\frac{\varepsilon_1^{core}+\varepsilon_2^{core}}{\varepsilon^{core}kd}\right)}\right]>0 \quad (1)$$

Here, ω_p^{3D}, γ_D, and k are the unscreened plasma frequency in three-dimensional (3D) bulk film, Drude damping coefficient, and the absolute value of the electron wave vector, respectively. With reduction in the thickness d, the repulsive KR potential among charges becomes independent of ε^{core}. In this case, the second term in parenthesis of Eq. 1 becomes proportional to $\left(\omega_p^{3D}\right)^2 \times kd$, which ultimately makes it less than one, and the material loses its ability to shield the incident electric field, completing its transition to the KR-insulator state (*19*).

Optical loss or ε'' in the TD-plasmonic and KR-insulating regime decreases with the reduced film thickness at long wavelengths (Fig. 1F). Such a decrease in ε'' originates from the reduced carrier concentration and increased damping in thinner films (see table S2). ε'' at ENZ wavelength increases substantially with decreasing film thickness from 150 to 4 nm due to increased γ_D (Fig. 1, G and H). Such an increase in γ_D with the decreasing film thickness appears because of a reduction in the electron mean free path owing to different scattering mechanisms. In ultrathin films, the main contribution to the damping not only originates from the increased electron-electron interactions but also could have contributions from surface roughness, electron-phonon, dislocations, and grain boundary scatterings. As electrons are confined progressively in thinner films, their ability to respond to the incident electric fields decreases, which not only reduces $|\varepsilon'|$ in the TD-plasmonic regime but also eventually leads to the MIT. The redshift in the ENZ wavelength or decrease in the ω_p in the TD-plasmonic regime is also associated with the vertical confinement of the electrons. Experimental results show a $\sqrt{d}$ dependence of $\omega_p(k)$ with the decreasing film thickness (*30*), which is consistent with the theoretical predictions (see section IIC in the Supplementary Materials for detailed discussion) (*19*, *23*).

Experimental reflection and transmission measurements verify the transition first from a Drude metal to a TD-plasmonic medium and then subsequent KR-insulator optical transition in HfN films. Reflection (and transmission) spectra of 15-nm-thin HfN film show a clear dip (and peak in transmission) at ~440 nm, near to its ENZ wavelength (Fig. 1, I and J). However, as the thickness of the film is reduced, the sharpness of the reflection dip, and, consequently, the transmission peak, becomes less prominent in the transdimensional (TD) films, as shown in fig. S2. Moreover, the reflection dip shifts to longer wavelengths to satisfy the impedance-matching conditions for redshifted plasma frequency in thinner films. The HfN film with 2 nm thickness exhibits a near constant ~98% transmission above ~550 nm that manifests its dielectric nature. Absorptions below 550 nm are associated with inter-band losses, as modeled using Lorentz oscillators. The optical images of HfN films (see inset in Fig. 1J) show the variation in transparency with changes in the film thickness. With their high transmission and conductive nature, ultrathin HfN films can be used as a transparent conducting electrode for smart windows, solar cells, wearables, and light-emitting diode applications. Note that, although the MgO substrate and superstrate (air) play an important role in the electron confinement and thereby influence the plasmonic properties of ultrathin metallic films, MgO substrates do not directly affect the optical and electrical measurements (see section VI in the Supplementary Materials).

Temperature-dependent dielectric permittivity provides further evidence for the three different optical regimes in HfN films. We observe that the $|\varepsilon'|$ of a thick HfN film decreases with the increasing temperature from 200 to 700 K while the ε'' increases because of the increased γ_D at high temperatures (see Fig. 2, A and B, and section IIH in the Supplementary Materials). In the TD-plasmonic regime (represented by the 5-nm-thick film), $|\varepsilon'|$ also decreases with the increasing temperature due to an increase in γ_D (*37*). Compared to the Drude metallic regime of HfN, the ε'' is decreasing to a lesser

degree at higher temperatures due to a near-constant ω_p. Such invariance of ω_p with the temperature is a unique feature of the TD-plasmonic medium and was earlier predicted theoretically (see section IIC in the Supplementary Materials for details) (*25*). Our finding is the experimental verification of this behavior where both 10-nm-thick and 4-nm-thick TD-plasmonic HfN films also show near-constant ω_p over the entire wavelength range (see Fig. 2C). In the KR-insulating regime (represented by the 2-nm film), ε' is positive throughout the temperature range and shows little variations. On the other hand, similar to the TD-plasmonic regime, the ε'' decreases slightly at higher temperatures, dropping from 17.5 to 11 at the wavelength of 2500 nm as the temperature increases from 200 to 700 K.

Thickness and temperature-dependent electronic transport measurements further correlate with the optical properties. Thick HfN film exhibits a low room temperature resistivity of 6.4×10^{-5} ohm·cm consistent with its metallic nature. However, as the thickness is reduced from 150 to 4 nm, resistivity increases by nearly five times in the TD-plasmonic regime at room temperature (see Fig. 3A). With a further reduction in thickness, resistivity increases markedly by more than three orders of magnitude in thinner films (<4 nm). Such a marked increase in resistivity suggests the onset of electronic confinement and a metal-insulator electronic transition, which correlates with the plasmonic breakdown in the ultrathin films. These results further suggests that, in the KR-insulating regime, large in-plane electronic interactions and the two-dimensional nature of the potential localize all states and E_F is below E_M as shown in Fig. 1C.

Consistent with resistivity, the carrier concentration (measured with the Hall experiment, see table S2) also decreases progressively in the TD-plasmonic regime but shows nearly two orders of magnitude decrease in ultrathin films (Fig. 3B). Within the Drude-metallic and TD-plasmonic regime, the variations of resistivity with thickness have been fitted with the dc-optical conductivity, considering modified dielectric permittivity (see section IIF in the Supplementary Materials) (*38*). As the insets show, the theoretical model matches the experiment results well. Note that even the most resistive film in the KR-insulating regime, 2-nm HfN, exhibits a resistivity of 2.41×10^{-1} ohm·cm (and carrier concentration of 3.70×10^{20} cm^{-3}) that is substantially lower in magnitude compared to the resistivity of other well-established band insulators such as SiO_2 and AlN (*39*, *40*).

Temperature-dependent (50 to 400 K) resistivity provides further evidence about the ensuring electronic and optical metal-to-insulator phase transition in HfN (see Fig. 3C). Thick 150-nm film, representing the Drude-metallic regime, shows a positive temperature coefficient of resistivity (TCR) typical for a good metal. The measured TCR of 0.9×10^{-3}/°C in HfN matches well with that of Au, Ag, Cu, and other metals (see table S8). As the thickness is reduced, initially, the films retain their positive TCR, such as in 10-nm film. However, the sign of TCR changes starting from 5-nm-thick film that exhibits a slight increase in the resistivity at low temperatures, highlighting the onset of electronic confinement. As the thickness is reduced further, the strength of confinement increases markedly for the 2.5- and 2-nm films as indicated by a pronounced increase in the resistivity at low temperatures and the nearly unchanged magnetoresistance (see fig. S6). The experimental resistivity-versus-temperature curves in thinner films are fitted with the nearest neighbor hopping and Mott variable range hopping model (MVRH) (*41*). Although the physical origin behind the localization of carriers is different in MVRH and the present case, the Mott temperature (T_M) provides a measure of the strength of confinement in the films (see section III in the Supplementary Materials). These results clearly show that, with shrinking thickness, HfN thin films undergo a metallic-to-insulating

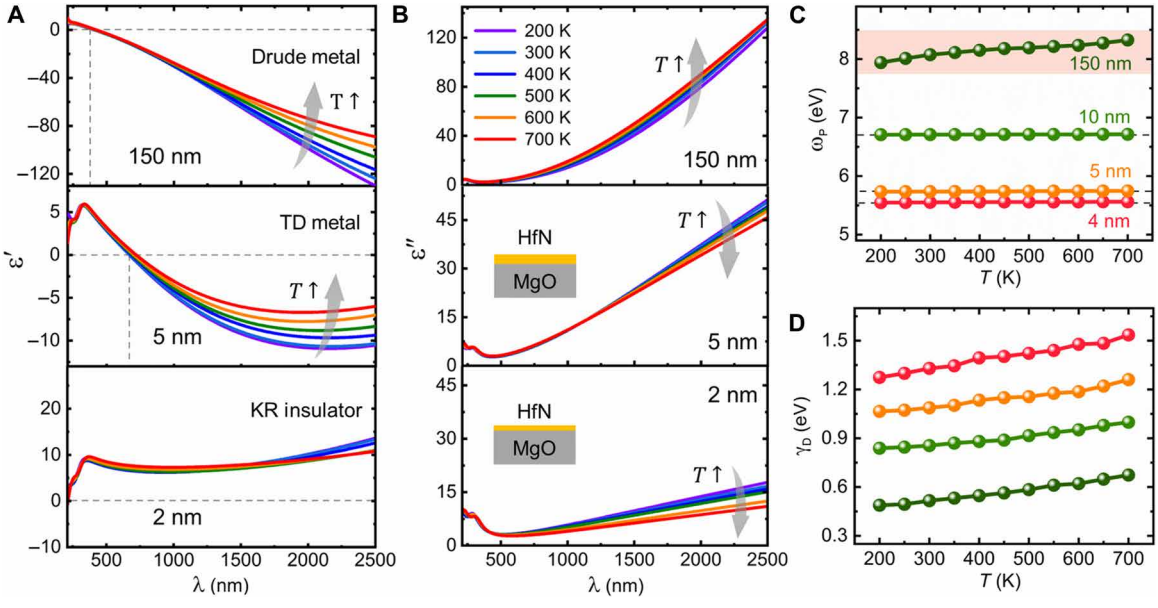

Fig. 2. Temperature-dependent dielectric permittivity of HfN across three different optical regimes. (**A**) Real (ε') and (**B**) imaginary (ε'') components of dielectric permittivity of HfN film as functions of temperature for three different thickness values—150, 5, and 2 nm—representing the Drude metallic, TD-plasmonic, and KR-insulator regimes, respectively. Temperature-dependent (**C**) plasma frequency and (**D**) Drude damping coefficient of HfN in the TD-plasmonic (with film thickness of 4, 5 nm, 10 nm) and Drude-metallic (150 nm) regime. For TD films, plasma frequency remains constant over a broad temperature range. However, the Drude damping coefficient increases with increase in temperature for all the films.

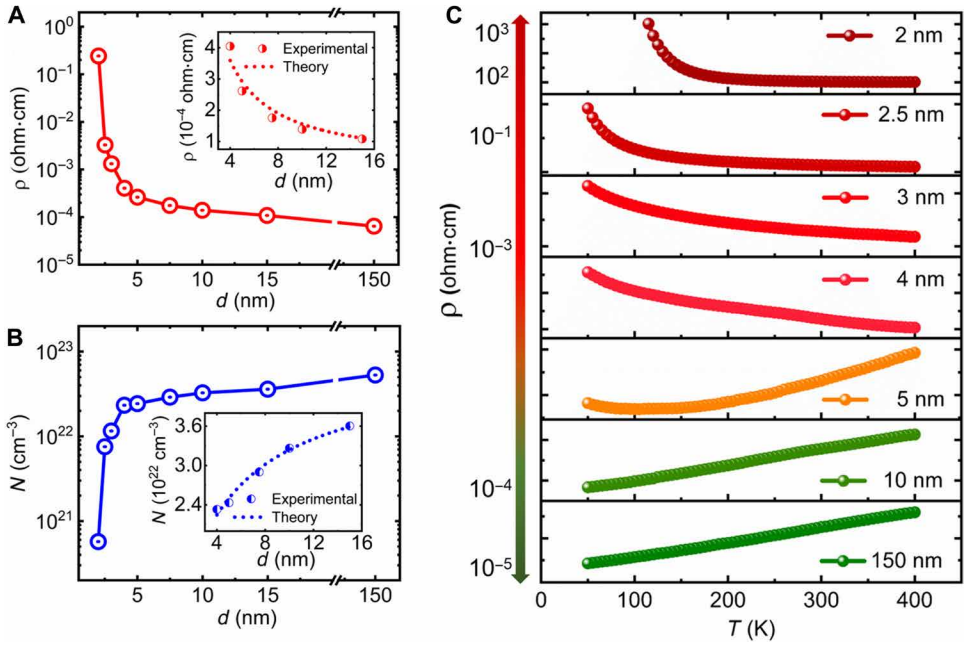

Fig. 3. Thickness-dependent electronic MITs in HfN films. Room temperature (**A**) electrical resistivity and (**B**) carrier concentration as a function of HfN film thickness. With decreasing thickness, resistivity increases and carrier concentration decreases. Insets show resistivity and carrier concentration in the TD-plasmonic regime that are fitted with theoretical equations S22 and S23 (see the Supplementary Materials). (**C**) Temperature-dependent electrical resistivity of films with different thicknesses. For 5-nm HfN film, a clear temperature-driven MIT is observed.

electronic transition with a colossal eight orders of magnitude increase in the resistivity at low temperatures in 2-nm-thick HfN film compared to that in 150-nm-thick film representing the bulk limit. Therefore, the electrical measurements reconcile the optical properties measured above and provide evidence for the breakdown of plasmon oscillations in HfN films.

Furthermore, using the repulsive KR interaction potential as the electrostatic interaction energy and the mean electron kinetic energy per particle as $\langle E_{kin}\rangle = \hbar^2\pi N_{2D}/(2m^*)$, where $N_{2D} = N_{3D}d = 1/(\pi\bar{\rho}^2)$ is the surface charge density, the dimensionless Platzman-Fukuyama (PF) ratio (*42*) of potential interaction energy and mean kinetic energy representing confinement strength is calculated as

$$\Gamma_0(\tilde{d},n) = \frac{1}{\bar{\varepsilon}\tilde{\varepsilon}\tilde{d}n}\left\{H_0\left(\frac{1}{\tilde{\varepsilon}\tilde{d}\sqrt{\pi n}}\right) - Y_0\left(\frac{1}{\tilde{\varepsilon}\tilde{d}\sqrt{\pi n}}\right)\right\} \quad (2)$$

where $\bar{\varepsilon} = \left(\varepsilon_1^{core} + \varepsilon_2^{core}\right)/2$; $\tilde{d} = d/a_B$ is the dimensionless thickness; $n = N_{2D}a_B^2 = N_{3D}da_B^2$ is the dimensionless surface density; H_0 and Y_0 are the Strove and Neumann functions, respectively; and $a_B = 0.529/2$ Å is the Bohr radius of the 2D hydrogen atom to set up the in-plane distance scale. Calculated $\Gamma_0(n, d)$ (see table S10) increases markedly as the thickness of the films and the corresponding carrier concentration decrease rapidly (Fig. 4A), which suggests a strong electron confinement in the TD plasmonic and KR insulator regimes. For the thinnest 2-nm HfN, $\Gamma_0(n, d)$ exceeds 1 satisfying the well-established PF condition for Wigner crystallization (*42*). These calculations suggest the exciting possibility of achieving Wigner crystallization (*40*, *41*) in TD materials (see section IV in the Supplementary Materials for details); however, its unambiguous experimental verification remains as a future avenue for research. Moreover, achieving $\Gamma_0(n, d)$ above 1 opens interesting opportunities to study strongly correlated regimes in TD materials, where several key parameters such as the electron density, the potential interaction energy, and the average kinetic energy can be tailored simply by changing the material thickness and dielectric environment.

First-principles density functional theory (DFT) calculations are used further to explain the role of electronic structure, phonons, and electron-phonon coupling on the optical responses of HfN and to model the dielectric response. The electronic structure of HfN shows that the valence band primarily comprises of N 2p states similar to other TMNs such as ScN (*43*, *44*), TiN (*45*), and CrN (*46*), while the conduction band exhibits Hf 5d characteristics (see Fig. 4B). The peak in ε'' at 5.63 eV in practically all HfN films corresponds to the inter-band transition from N 2p to Hf 5d, from valence band to the unoccupied conduction band at the Γ point, as shown in Fig. 1F. Although the conventional DFT calculations cannot incorporate the electron confinement effects in thinner films (*47*, *48*), a comparison of the electronic densities of states in bulk and a bilayer of HfN provides important insight. As presented in Fig. 4C, the valence bandwidth and the distance of the valence band tail from E_F are lower in thinner films than those in the bulk HfN. Because localization generally sets in from the band tails, the narrower bands close to the E_F facilitate the electronic confinement (*49*). In addition, time-dependent–density functional perturbation theory calculations that model the dielectric constants show that the experimental ε' and ε'' can be well captured for the bulk HfN with a low concentration of Hf vacancies (see section V in the Supplementary Materials) (*50*).

Last, high-resolution x-ray diffraction (HRXRD) and transmission electron microscopy imaging evidence the structural quality of the HfN films. Figure 4D shows a symmetric 2θ–ω HRXRD 002 peak of thick HfN representing a lattice constant of 4.52 Å,

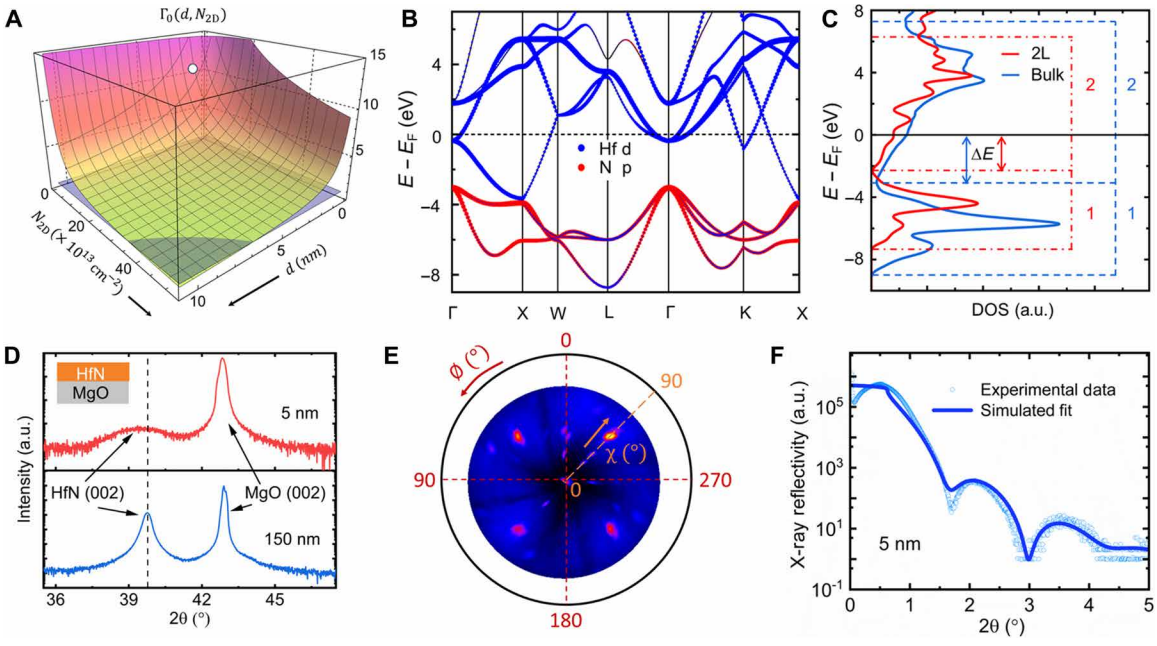

Fig. 4. Theoretical calculations and structural characterization of HfN. (**A**) $\Gamma_0(n, d)$ calculated with KR interacting potential and with experimental parameters at room temperature shows greater than 1 value for 2-nm-thick HfN (a dot in the image). (**B**) Projected electronic band structure of HfN with d orbitals of Hf (blue) and p orbitals of N (red). (**C**) Electronic density of states for two-layer (2L) (red) and bulk (sky blue) HfN. Dashed lines represent the energy position of the two bands (labeled by 1 and 2) with respect to the Fermi level (E_F). (**D**) High-resolution x-ray diffraction (HRXRD) of 5- and 150-nm HfN films deposited on (001) MgO substrates. (**E**) Pole figure corresponding to the (111) reflection and (**F**) x-ray reflectivity (XRR) spectra of the epitaxial 5-nm film along with the fitting are presented that highlight uniform and coherent epitaxial growth. a.u., arbitrary units.

consistent with its bulk values (*51*). Although the 002 HRXRD peaks are broader in thinner films due to the presence of residual strain, they maintain their layer coherency and epitaxy as evidenced in the pole figure mapping (Fig. 4E) as well as x-ray reflectivity (XRR) analysis (Fig. 4F). High-angle annular dark-field scanning transmission electron microscopy images (see fig. S21) show cube-on-cube growth of (002) HfN on (001) MgO substrates with an epitaxial relationship [001] (001) HfN || [001] (001) MgO substrates. Further details on the structural characterizations are presented in the Supplementary Materials.

In summary, we present the conclusive experimental evidence of electron confinement–induced plasmonic breakdown and an MIT in an archetypal ultrathin refractory plasmonic metal, HfN. The strong in-plane Coulomb interaction among charges in transdimensional HfN films leads to a spatial dispersion of its plasma frequency and a higher Drude damping coefficient. This results in electrons losing their ability to screen the incident electronic field, transforming the material into a dielectric. The experimental observations are explained by nonlocal dielectric response theory based on the KR potential. The breakdown of plasmon resonance in ultrathin HfN is analogous to dielectric breakdown in insulators and could enable innovative active metasurface and metamaterial concepts, where electron confinement is used to tune the optical properties of plasmonic materials. The plasmon resonance breakdown and MIT are intrinsic to all ultrathin plasmonic materials, with subtle differences due to the properties of the materials themselves, as well as the substrate and superstrate. Furthermore, this approach could be used to study advanced physics in strongly correlated regimes in transdimensional materials.

MATERIALS AND METHODS

Growth details

HfN films are deposited on (001) MgO substrate (1 cm by 1 cm) inside an ultrahigh vacuum chamber with a base pressure of 1×10^{-9} torr using a reactive dc magnetron sputtering system (PVD Products Inc.). The Hf target has the dimensions of 2 inches (5.08 cm) in diameter and 0.25 inches (0.635 cm) in thickness. Before the deposition, substrates are cleaned with acetone and methanol for 15 min. HfN films with different thicknesses are deposited at a pressure of 5 mtorr maintaining an $Ar:N_2$ gas mixture ratio of 9:2 standard cubic centimeter per minute. During the deposition, the target power and the substrate temperature are maintained at a constant 100 W and 900°C, respectively. For the transmission measurements, HfN films are also deposited on double-sided polished quartz substrate along with the (001) MgO substrates. This work represents the nanofabrication of ultrathin HfN films.

Ellipsometry measurements

The optical properties of HfN films are measured in reflection mode at three different incident angles (55°, 65°, and 75°) using a variable angle spectroscopic ellipsometer (VASE) (J.A. Woollam Co.). The experimental Psi (ψ) and Delta (Δ) spectra were fitted using a Drude-Lorentz oscillator model in CompleteEASE software. Temperature-dependent optical properties are measured from 200 to 700 K at 70° angle of incidence using a vacuum-based cryostat attached with the ellipsometer. Angle-dependent reflection and transmission measurements are also performed with the VASE machine. Dielectric permittivities are extracted from the fitting of experimental ψ and Δ spectra with the Drude and Lorentz oscillator

model. The Drude term considers the contribution from conduction electrons and the Lorentz term corresponds to the inter-band transitions. The total permittivity can be expressed as

$$\varepsilon = \varepsilon' + i\varepsilon'' = \varepsilon_{\text{core}} - \frac{\omega_p^2}{\omega^2 + i\gamma_D\omega} + \sum_{j=1}^{2} \frac{\omega_{l,j}^2}{\omega_{0,j}^2 - \omega^2 - i\gamma_j\omega} \quad (3)$$

where ε_{core}, ω_p, and γ_D are core dielectric constant, unscreened plasma frequency, and the Drude damping coefficient, respectively. $\omega_{l,j}^2 = f_j\omega_{0,j}\gamma_j$, where f_j, $\omega_{0,j}$, and γ_j describe the Lorentz oscillator strength, resonant energy, and the damping coefficient, respectively. The unscreened plasma frequency is given by the formula, $\omega_p = \sqrt{\frac{4\pi Ne^2}{m^*\varepsilon_0}}$, whereas the screened plasma frequency depends on the core dielectric constant (ε^{core}) of the medium, $\omega_p = \sqrt{\frac{4\pi Ne^2}{m^*\varepsilon^{core}}}$. Here, N, m^*, and ε_0 are the electron concentration, effective mass, and free space permittivity, respectively. From the fitting procedure standpoint, the relative percentage errors in the plasma frequency and Drude damping constants are ±1%.

Transmission measurements

Normal transmission measurements are performed from 200 to 2500 nm spectral range using a Cary 5000 Agilent UV-Vis-NIR spectrophotometer. The substrate (quartz) is used as a baseline for the measurement.

Electrical resistivity measurements

Room temperature electrical resistivity and electron concentrations of the HfN films are measured using the Ecopia HMS-3000 Hall measurement system. Temperature-dependent electrical resistivity measurements are performed from 50 to 400 K in standard four-probe geometry using a cryogen-free quantum device physical property measurement system. The estimated error in the resistivity and carrier concentration measurement is ±1%.

Structural characterizations

HRXRD is performed with Rigaku SmartLab x-ray diffractometer. The rotating anode x-ray generator is set at 4.5 kW during the measurement. Parallel beam optics with a multilayer x-ray mirror, a Germanium (220) two-bounce channel cut monochromator, and a Germanium (220) two-bounce analyzer are used for the measurement. XRR fitting was performed with SmartLab software using Parratt formalism.

Supplementary Materials

This PDF file includes:

Supplementary Text
Figs. S1 to S22
Tables S1 to S14
References

REFERENCES AND NOTES

1. A. Polman, H. A. Atwater, Plasmonics: Optics at the nanoscale. *Mater. Today* **8**, 56 (2005).
2. M. L. Brongersma, V. M. Shalaev, The case for plasmonics. *Science* **328**, 440–441 (2010).
3. N. I. Zheludev, Y. S. Kivshar, From metamaterials to metadevices. *Nat. Mater.* **11**, 917–924 (2012).
4. T. W. Ebbesen, C. Genet, S. I. Bozhevolnyi, Surface-plasmon circuitry. *Phys. Today* **61**, 44–50 (2008).
5. N. J. Halas, S. Lal, W.-S. Chang, S. Link, P. Nordlander, Plasmons in strongly coupled metallic nanostructures. *Chem. Rev.* **111**, 3913–3961 (2011).
6. X. Zhang, Y. L. Chen, R.-S. Liu, D. P. Tsai, Plasmonic photocatalysis. *Rep. Prog. Phys.* **76**, 046401 (2013).
7. U. Guler, J. C. Ndukaife, G. V. Naik, A. G. A. Nnanna, A. V. Kildishev, V. M. Shalaev, A. Boltasseva, Local heating with lithographically fabricated plasmonic titanium nitride nanoparticles. *Nano Lett.* **13**, 6078–6083 (2013).
8. H. A. Atwater, A. Polman, Plasmonics for improved photovoltaic devices. *Nat. Mater.* **9**, 205–213 (2010).
9. J. Homola, S. S. Yee, G. Gauglitz, Surface plasmon resonance sensors: Review. *Sens. Actuators B Chem.* **54**, 3–15 (1999).
10. F. J. García de Abajo, Optical excitations in electron microscopy. *Rev. Mod. Phys.* **82**, 209–275 (2010).
11. J. Leuthold, C. Hoessbacher, S. Muehlbrandt, A. Melikyan, M. Kohl, C. Koos, W. Freude, V. Dolores-Calzadilla, M. Smit, I. Suarez, J. Martínez-Pastor, E. P. Fitrakis, I. Tomkos, Plasmonic communications: Light on a wire. *Opt. Photonics News* **24**, 28–35 (2013).
12. M. Kauranen, A. V. Zayats, Nonlinear plasmonics. *Nat. Photonics* **6**, 737–748 (2012).
13. J.-Y. Bigot, V. Halté, J.-C. Merle, A. Daunois, Electron dynamics in metallic nanoparticles. *Chem. Phys.* **251**, 181–203 (2000).
14. H. Y. Li, S. M. Zhou, J. Li, Y. L. Chen, S. Y. Wang, Z. C. Shen, L. Y. Chen, H. Liu, X. X. Zhang, Analysis of the drude model in metallic films. *Appl. Optics* **40**, 6307–6311 (2001).
15. K. C. Maurya, D. Rao, S. Acharya, P. Rao, A. I. K. Pillai, S. K. Selvaraja, M. Garbrecht, B. Saha, Polar semiconducting scandium nitride as an infrared plasmon and phonon–polaritonic material. *Nano Lett.* **22**, 5182–5190 (2022).
16. A. N. Grigorenko, M. Polini, K. S. Novoselov, Graphene plasmonics. *Nat. Photonics* **6**, 749–758 (2012).
17. Q. Ouyang, S. Zeng, L. Jiang, L. Hong, G. Xu, X.-Q. Dinh, J. Qian, S. He, J. Qu, P. Coquet, K.-T. Yong, Sensitivity enhancement of transition metal dichalcogenides/silicon nanostructure-based surface plasmon resonance biosensor. *Sci. Rep.* **6**, 28190 (2016).
18. L. V. Keldysh, Coulomb interaction in thin semiconductor and semimetal films. *JETP Lett.* **29**, 658–661 (1980).
19. I. V. Bondarev, V. M. Shalaev, Universal features of the optical properties of ultrathin plasmonic films. *Opt. Mater. Express* **7**, 3731–3740 (2017).
20. X. Li, C. H. Tung, K. L. Pey, The nature of dielectric breakdown. *Appl. Phys. Lett.* **93**, 072903 (2008).
21. Z. M. Abd El-Fattah, V. Mkhitaryan, J. Brede, L. Fernández, C. Li, Q. Guo, A. Ghosh, A. R. Echarri, D. Naveh, F. Xia, J. E. Ortega, F. J. García de Abajo, Plasmonics in atomically thin crystalline silver films. *ACS Nano* **13**, 7771–7779 (2019).
22. V. Caligiuri, M. Palei, M. Imran, L. Manna, R. Krahne, Planar double-epsilon-near-zero cavities for spontaneous Emission and Purcell effect enhancement. *ACS Photonics* **5**, 2287–2294 (2018).
23. I. V. Bondarev, H. Mousavi, V. M. Shalaev, Optical response of finite-thickness ultrathin plasmonic films. *MRS Commun.* **8**, 1092–1097 (2018).
24. I. V. Bondarev, C. M. Adhikari, Collective excitations and optical response of ultrathin carbon-nanotube films. *Phys. Rev. Appl.* **15**, 034001 (2021).
25. L. Vertchenko, L. Leandro, E. Shkondin, O. Takayama, I. V. Bondarev, N. Akopian, A. V. Lavrinenko, Cryogenic characterization of titanium nitride thin films. *Opt. Mater. Express* **9**, 2117–2127 (2019).
26. H. Salihoglu, J. Shi, Z. Li, Z. Wang, X. Luo, I. V. Bondarev, S.-A. Biehs, S. Shen, Nonlocal near-field radiative heat transfer by transdimensional plasmonics. *Phys. Rev. Lett.* **131**, 086901 (2023).
27. A. Kossoy, V. Merk, D. Simakov, K. Leosson, S. Kéna-Cohen, S. A. Maier, Optical and structural properties of ultra-thin gold films. *Adv. Opt. Mater.* **3**, 71–77 (2015).
28. G. V. Naik, V. M. Shalaev, A. Boltasseva, Alternative plasmonic materials: Beyond gold and silver. *Adv. Mater.* **25**, 3264–3294 (2013).
29. C. M. Zgrabik, E. L. Hu, Optimization of sputtered titanium nitride as a tunable metal for plasmonic applications. *Opt. Mater. Express* **5**, 2786–2797 (2015).
30. D. Shah, M. Yang, Z. Kudyshev, X. Xu, V. M. Shalaev, I. V. Bondarev, A. Boltasseva, Thickness-dependent drude plasma frequency in transdimensional plasmonic TiN. *Nano Lett.* **22**, 4622–4629 (2022).
31. D. Shah, H. Reddy, N. Kinsey, V. M. Shalaev, A. Boltasseva, Optical properties of plasmonic ultrathin TiN films. *Adv. Opt. Mater.* **5**, 1700065 (2017).
32. A. B. Mei, A. Rockett, L. Hultman, I. Petrov, J. E. Greene, Electron/phonon coupling in group-IV transition-metal and rare-earth nitrides. *J. Appl. Phys.* **114**, 193708 (2013).
33. P. Das, B. Biswas, K. C. Maurya, M. Garbrecht, B. Saha, Refractory plasmonic hafnium nitride and zirconium nitride thin films as alternatives to silver for solar mirror applications. *ACS Appl. Mater. Interfaces* **14**, 46708–46715 (2022).
34. S. Chung, X. Wen, S. Huang, N. Gupta, G. Conibeer, S. Shrestha, T. Harada, T. W. Kee, Nanosecond long excited state lifetimes observed in hafnium nitride. *Sol. Energy Mater. Sol. Cells* **169**, 13–18 (2017).
35. S. Chakraborty, H. Uchiyama, M. Garbrecht, V. Bhatia, A. I. K. Pillai, J. P. Feser, D. T. Adroja, S. Langridge, B. Saha, Phononic bandgap and phonon anomalies in HfN and HfN/ScN metal/semiconductor superlattices measured with inelastic x-ray scattering. *Appl. Phys. Lett.* **117**, 111901 (2020).

36. P. Das, K. C. Maurya, J. L. Schroeder, M. Garbrecht, B. Saha, Near-UV-to-Near-IR hyperbolic photonic dispersion in epitaxial (Hf,Zr)N/ScN metal/dielectric superlattices. *ACS Appl. Energy Mater.* **5**, 3898–3904 (2022).
37. H. Reddy, U. Guler, Z. Kudyshev, A. V. Kildishev, V. M. Shalaev, A. Boltasseva, Temperature-dependent optical properties of plasmonic titanium nitride thin films. *ACS Photonics* **4**, 1413–1420 (2017).
38. H. Van Bui, A. Y. Kovalgin, R. A. M. Wolters, On the difference between optically and electrically determined resistivity of ultra-thin titanium nitride films. *Appl. Surf. Sci.* **269**, 45–49 (2013).
39. K. M. Taylor, C. Lenie, Some properties of aluminum nitride. *J. Electrochem. Soc.* **107**, 308 (1960).
40. H. Bartzsch, D. Glöß, B. Böcher, P. Frach, K. Goedicke, Properties of SiO_2 and Al_2O_3 films for electrical insulation applications deposited by reactive pulse magnetron sputtering. *Surf. Coatings Technol.* **174-175**, 774–778 (2003).
41. M. Roy, N. R. Mucha, S. Fialkova, D. Kumar, Effect of thickness on metal-to-semiconductor transition in 2-dimensional TiN thin films. *AIP Adv.* **11**, 045204 (2021).
42. P. M. Platzman, H. Fukuyama, Phase diagram of the two-dimensional electron liquid. *Phys. Rev. B* **10**, 3150–3158 (1974).
43. D. Mukhopadhyay, S. Rudra, B. Biswas, P. Das, B. Saha, Surface scattering-dependent electronic transport in ultrathin scandium nitride films. *Appl. Phys. Lett.* **123**, 192101 (2023).
44. S. Rudra, D. Rao, S. Poncé, B. Saha, Reversal of band-ordering leads to high hole mobility in strained *p* -type Scandium nitride. *Nano Lett.* **23**, 8211–8217 (2023).
45. A. Catellani, A. Calzolari, Plasmonic properties of refractory titanium nitride. *Phys. Rev. B* **95**, 115145 (2017).
46. B. Biswas, S. Rudra, R. S. Rawat, N. Pandey, S. Acharya, A. Joseph, A. I. K. Pillai, M. Bansal, M. de H-Óra, D. P. Panda, A. B. Dey, F. Bertram, C. Narayana, J. MacManus-Driscoll, T. Maity, M. Garbrecht, B. Saha, Magnetic stress-driven metal-insulator transition in strongly correlated antiferromagnetic CrN. *Phys. Rev. Lett.* **131**, 126302 (2023).
47. P. Mori-Sánchez, A. J. Cohen, W. Yang, Localization and delocalization errors in density functional theory and implications for band-gap Prediction. *Phys. Rev. Lett.* **100**, 146401 (2008).
48. H. Jiang, First-principles approaches for strongly correlated materials: A theoretical chemistry perspective. *Int. J. Quantum Chem.* **115**, 722–730 (2015).
49. J. F. Wager, Real- and reciprocal-space attributes of band tail states. *AIP Adv.* **7**, 125321 (2017).
50. I. Timrov, N. Vast, R. Gebauer, S. Baroni, turboEELS—A code for the simulation of the electron energy loss and inelastic X-ray scattering spectra using the Liouville–Lanczos approach to time-dependent density-functional perturbation theory. *Comput. Phys. Commun.* **196**, 460–469 (2015).
51. B. Saha, J. Acharya, T. D. Sands, U. V. Waghmare, Electronic structure, phonons, and thermal properties of ScN, ZrN, and HfN: A first-principles study. *J. Appl. Phys.* **107**, 033715 (2010).
52. K. C. Maurya, V. M. Shalaev, A. Boltasseva, B. Saha, Reduced optical losses in refractory plasmonic titanium nitride thin films deposited with molecular beam epitaxy. *Opt. Mater. Express* **10**, 2679–2692 (2020).
53. I. V. Bondarev, H. Mousavi, V. M. Shalaev, Transdimensional epsilon-near-zero modes in planar plasmonic nanostructures. *Phys. Rev. Res.* **2**, 013070 (2020).
54. H. Reddy, U. Guler, A. V. Kildishev, A. Boltasseva, V. M. Shalaev, Temperature-dependent optical properties of gold thin films. *Opt. Mater. Express* **6**, 2776–27802 (2016).
55. H. Reddy, U. Guler, K. Chaudhuri, A. Dutta, A. V. Kildishev, V. M. Shalaev, A. Boltasseva, Temperature-dependent optical properties of single crystalline and polycrystalline silver thin films. *ACS Photonics* **4**, 1083–1091 (2017).
56. J. Liao, Y. Ou, X. Feng, S. Yang, C. Lin, W. Yang, K. Wu, K. He, X. Ma, Q.-K. Xue, Y. Li, Observation of Anderson localization in ultrathin films of three-dimensional topological insulators. *Phys. Rev. Lett.* **114**, 216601 (2015).
57. P. Giannozzi, O. Andreussi, T. Brumme, O. Bunau, M. B. Nardelli, M. Calandra, R. Car, C. Cavazzoni, D. Ceresoli, M. Cococcioni, N. Colonna, I. Carnimeo, A. D. Corso, S. de Gironcoli, P. Delugas, R. A. DiStasio Jr., A. Ferretti, A. Floris, G. Fratesi, G. Fugallo, R. Gebauer, U. Gerstmann, F. Giustino, T. Gorni, J. Jia, M. Kawamura, H.-Y. Ko, A. Kokalj, E. Küçükbenli, M. Lazzeri, M. Marsili, N. Marzari, F. Mauri, N. L. Nguyen, H.-V. Nguyen, A. Otero-de-la-Roza, L. Paulatto, S. Poncé, D. Rocca, R. Sabatini, B. Santra, M. Schlipf, A. P. Seitsonen, A. Smogunov, I. Timrov, T. Thonhauser, P. Umari, N. Vast, X. Wu, S. Baroni, Advanced capabilities for materials modelling with Quantum ESPRESSO. *J. Phys. Condens. Matter* **29**, 465901 (2017).
58. J. P. Perdew, K. Burke, M. Ernzerhof, Generalized gradient approximation made simple. *Phys. Rev. Lett.* **77**, 3865–3868 (1996).
59. D. Vanderbilt, Soft self-consistent pseudopotentials in a generalized eigenvalue formalism. *Phys. Rev. B Condens. Matter* **41**, 7892–7895 (1990).
60. N. Troullier, J. L. Martins, Efficient pseudopotentials for plane-wave calculations. *Phys. Rev. B Condens. Matter* **43**, 1993–2006 (1991).
61. M. Schlipf, F. Gygi, Optimization algorithm for the generation of ONCV pseudopotentials. *Comput. Phys. Commun.* **196**, 36–44 (2015).
62. M. Methfessel, A. T. Paxton, High-precision sampling for Brillouin-zone integration in metals. *Phys. Rev. B* **40**, 3616–3621 (1989).
63. N. Marzari, D. Vanderbilt, A. De Vita, M. C. Payne, Thermal contraction and disordering of the Al(110) surface. *Phys. Rev. Lett.* **82**, 3296–3299 (1999).
64. I. Timrov, M. Markov, T. Gorni, M. Raynaud, O. Motornyi, R. Gebauer, S. Baroni, N. Vast, Ab initio study of electron energy loss spectra of bulk bismuth up to 100 eV. *Phys. Rev. B* **95**, 094301 (2017).
65. I. Timrov, N. Vast, R. Gebauer, S. Baroni, Electron energy loss and inelastic x-ray scattering cross sections from time-dependent density-functional perturbation theory. *Phys. Rev. B* **88**, 064301 (2013).
66. G. Prandini, M. Galante, N. Marzari, P. Umari, SIMPLE code: Optical properties with optimal basis functions. *Comput. Phys. Commun.* **240**, 106–119 (2019).
67. O. Motornyi, N. Vast, I. Timrov, O. Baseggio, S. Baroni, A. Dal Corso, Electron energy loss spectroscopy of bulk gold with ultrasoft pseudopotentials and the Liouville-Lanczos method. *Phys. Rev. B* **102**, 035156 (2020).
68. H. Maurilio, L. Carvalho, M. Rebello, S. Dias, A. T. Bezerra, Anisotropic optical response of gold-silver alloys. *Res. Sq.* 10.21203/rs.3.rs-711773/v1 (2021).
69. T. Rangel, D. Kecik, P. E. Trevisanutto, G.-M. Rignanese, H. Van Swygenhoven, V. Olevano, Band structure of gold from many-body perturbation theory. *Phys. Rev. B* **86**, 125125 (2012).
70. S. Li, A. Wang, Y. Hu, X. Gu, Z. Tong, H. Bao, Anomalous thermal transport in metallic transition-metal nitrides originated from strong electron–phonon interactions. *Mater. Today Phys.* **15**, 100256 (2020).
71. A. N. Christensen, W. Kress, M. Miura, N. Lehner, Phonon anomalies in transition-metal nitrides: HfN. *Phys. Rev. B* **28**, 977–981 (1983).
72. D. Gall, The search for the most conductive metal for narrow interconnect lines. *J. Appl. Phys.* **127**, 050901 (2020).
73. K. Balasubramanian, S. V. Khare, D. Gall, Energetics of point defects in rocksalt structure transition metal nitrides: Thermodynamic reasons for deviations from stoichiometry. *Acta Mater.* **159**, 77–88 (2018).
74. D. Shah, A. Catellani, H. Reddy, N. Kinsey, V. Shalaev, A. Boltasseva, A. Calzolari, Controlling the plasmonic properties of ultrathin TiN films at the atomic level. *ACS Photonics* **5**, 2816–2824 (2018).

Acknowledgments: P.D. and B.S. acknowledge the International Centre for Materials Science (ICMS) and Sheikh Saqr Laboratory (SSL) of Jawaharlal Nehru Centre for Advanced Scientific Research (JNCASR) for support. P.D., D.R., and B.S. acknowledge the SAMat Research Facilities, JNCASR, Bengaluru. S.R. and B.S. acknowledged the PARAM Yukti supercomputing facility under the national supercomputing mission of India at JNCASR, Bengaluru, for providing computational resources. M.G. and A.I.K.P. acknowledge the facilities of Sydney Microscopy and Microanalysis at the University of Sydney. P.D. thanks B. Biswas for various scientific discussions. **Funding:** This work was supported by the funding from the Ras Al Khaimah Centre for Advanced Materials and Raknor LLC; Young Scientist Research Award (YSRA) from the Board of Research in Nuclear Sciences (BRNS); and Department of Atomic Energy (DAE), India, with grant number 59/20/10/2020-BRNS/59020. P.D., S.R., and S.B. thank the Council of Scientific and Industrial Research for the fellowship. D.R. thanks JNCASR for the fellowship. I.V.B. acknowledges support from the US Army Research Office under award no. W911NF2310206. A.B. and V.M.S. acknowledge support by the US Department of Energy, Office of Basic Energy Sciences, Division of Materials Sciences and Engineering, under award DE-SC0017717 and Air Force Office of Scientific Research (AFOSR) under award FA9550-20-1-0124. **Author contributions:** Conceptualization: P.D., S.R., M.G., A.B., I.V.B., V.M.S., and B.S. Sample preparation: P.D. Measurements and data analysis: P.D., D.R., and S.B. Theoretical computation: S.R. and I.V.B. TEM sample preparation: A.I.K.P. TEM imaging and analysis: M.G. Writing—original draft: P.D., S.R., M.G., V.M.S., and B.S. Writing—review and editing: P.D., S.R., S.B., A.I.K.P., M.G., A.B., I.V.B., V.M.S., and B.S. Supervision: A.B. and B.S. **Competing interests:** The authors declare that they have no competing interests. **Data and materials availability:** All data needed to evaluate the conclusions in the paper are present in the paper and/or the Supplementary Materials.

Submitted 22 June 2024
Accepted 16 October 2024
Published 20 November 2024
10.1126/sciadv.adr2596